

Ultrastructures and Mechanics of Annealed *Nephila clavipes* Major Ampullate Silk

T. W. Duggar, M. Zhernenkov

To be published in "BIO MACROMOLECULES"

January 2020

Photon Sciences

Brookhaven National Laboratory

U.S. Department of Energy

USDOE Office of Science (SC), Basic Energy Sciences (BES) (SC-22)

Notice: This manuscript has been authored by employees of Brookhaven Science Associates, LLC under Contract No. DE-SC0012704 with the U.S. Department of Energy. The publisher by accepting the manuscript for publication acknowledges that the United States Government retains a non-exclusive, paid-up, irrevocable, world-wide license to publish or reproduce the published form of this manuscript, or allow others to do so, for United States Government purposes.

DISCLAIMER

This report was prepared as an account of work sponsored by an agency of the United States Government. Neither the United States Government nor any agency thereof, nor any of their employees, nor any of their contractors, subcontractors, or their employees, makes any warranty, express or implied, or assumes any legal liability or responsibility for the accuracy, completeness, or any third party's use or the results of such use of any information, apparatus, product, or process disclosed, or represents that its use would not infringe privately owned rights. Reference herein to any specific commercial product, process, or service by trade name, trademark, manufacturer, or otherwise, does not necessarily constitute or imply its endorsement, recommendation, or favoring by the United States Government or any agency thereof or its contractors or subcontractors. The views and opinions of authors expressed herein do not necessarily state or reflect those of the United States Government or any agency thereof.

Ultrastructures and Mechanics of Annealed *Nephila clavipes* Major Ampullate Silk

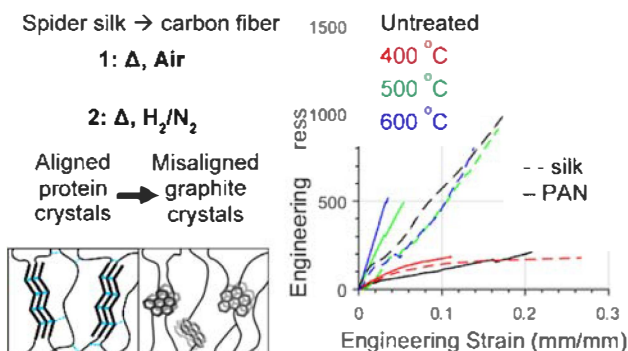
Thomas W. Dugger, Sourangsu Sarkar, Sandra M. Correa-Garhwal, Mikhail Zhernenkov, Yugang Zhang, Gitanjali Kolhatkar, Ramya Mohan, Luz Cruz, Aura D. Lubio, Andreas Ruediger, Cheryl Y. Hayashi, Kathryn E. Uhrich, and David J. Kisailus*

ABSTRACT: The semicrystalline protein structure and impressive mechanical properties of major ampullate (MA) spider silk make it a promising natural alternative to polyacrylonitrile (PAN) fibers for carbon fiber manufacture. However, when annealed using a similar procedure to carbon fiber production, the tensile strength and Young's modulus of MA silk decrease. Despite this, MA silk fibers annealed at 600 °C remain stronger and tougher than similarly annealed PAN but have a lower Young's modulus. Although MA silk and PAN graphitize to similar extents, annealing disrupts the hydrogen bonding that controls crystal alignment within MA silk. Consequently, unaligned graphite crystals form in annealed MA silk, causing it to weaken, while graphite crystals in PAN maintain alignment along the fiber axis, strengthening the fibers. These shortcomings of spider silk when annealed provide insights into the selection and design of future alternative carbon fiber precursors.

1. INTRODUCTION

Carbon fiber-reinforced composites are finding increased use in structural applications because of their low density and comparable stiffness, toughness, and strength to aluminum.^{1,2} Carbon fibers are commonly manufactured from polyacrylonitrile (PAN) fiber precursors that are wet-spun from organic solvents such as *N,N*-dimethylformamide and subsequently oxidized, carbonized, and graphitized at temperatures up to 3000 °C.^{3,4} During oxidation in air, nitrile groups react with the hydrocarbon backbone to form chains of semiaromatic nitrogen-containing rings in a process called cyclization.⁵ The oxidized fibers are then carbonized through annealing in an inert or reducing environment at temperatures up to 1000 °C, where the adjacent cyclized chains fuse together through dehydrogenation and nitrogen loss to form graphite crystals.⁶ This chain fusion continues during the graphitization process at above 1000 °C, where the graphite crystal size and carbon fiber mechanical properties are directly proportional to the annealing temperature.⁶ The high temperatures, toxic precursors, and toxic solvents required make PAN-based carbon fiber production an expensive and environmentally unfriendly process; consequently, researchers have investigated natural fibers as alternate precursors, but these fibers consistently produce weaker carbon fiber than PAN.⁷⁻⁹

Spiders create silk fibers made mostly of structural silk proteins called spidroins (spider fibroins), which fold into



parallel nanofibrils along the length of the fiber.^{10,11} With a toughness comparable to synthetic rubbers and a yield strength 1/3rd that of Kevlar fiber, dragline silk from the major ampullate (MA) gland (MA silk) has been extensively studied in hopes of creating synthetic silk analogues or reproducing elements of silk protein structures in biomimetic polymer fibers.¹² MA silk's strength is largely associated with polyaniline β -sheet nanocrystals interconnected by hydrogen bonds, which can break and reform under loading.¹³ These nanocrystals are preferentially aligned along the long axis of the fiber and theorized as natural templates for graphite crystal formation upon annealing.^{14,15} Cho et al. showed that MA silk graphitizes upon annealing, but to date, the strength and stiffness of MA silk and PAN-based carbon fiber have not been directly compared.¹⁵ This study investigates the ultrastructure and mechanics of *Nephila clavipes* (golden silk orb-weaver, recently renamed as *Trichonephila clavipes*¹⁶) MA silk after it is oxidized and annealed using a procedure similar to the oxidation and carbonization of PAN.

2. EXPERIMENTAL SECTION

2.1. Thermal Treatment and Characterization. Female *N. clavipes* were collected from the southeastern United States and housed in 24 × 24 × 5 cm plexiglass cages. They were fed a diet of commercially available crickets and misted with water twice a week. MA silk was collected through forced silking at a rate of 1 cm/s; prior to silking, each spider was anesthetized with CO₂ for 5 min. Chopped PAN fibers were purchased from Smooth On Inc., and poly(L-alanine) powder was purchased from Millipore Sigma. PAN fibers and MA silk fiber bundles were oxidized in 100 cm³ of air at 275 °C for 1 h at a ramp rate of 2.5 °C/min in a tube furnace (Lindberg Blue M, Thermo Fisher Scientific, USA). Some oxidized fibers were set aside for characterization. For the annealing step, room temperature oxidized fibers were further heated at 400, 500, and 600 °C for 1 h at 2.5 °C/min in 100 cm³ of a reducing 5% H₂/N₂ atmosphere that is chosen instead of an inert atmosphere to catalyze carbonization within the fibers. When annealed under tension, as is commonly done in carbon fiber manufacture, ~75% of the MA silk fibers broke. Thus, MA silk fibers were given 30–50% of their length in slack when oxidized and annealed, and PAN fibers were annealed freestanding for consistency. The 2.5 °C/min heating rate was also chosen to minimize fiber breaking during annealing.

Single MA silk fibers for tensile testing were secured to pieces of aluminum foil with high temperature-stable Pyro-Putty (Aremco) adhesive, and then oxidized and annealed following the same process. Fiber bundle masses before and after oxidation and annealing were measured using a Mettler-Toledo XS 104 balance. Because of the time-intensive process to collect MA silk, the mass change was measured on 0.5–1 mg bundles of MA silk, while PAN fiber bundle masses were 10–100 mg. Thermogravimetric analysis (TGA) was performed on a Mettler-Toledo TGA/DSC 3+ following the same oxidation and annealing procedures but using 125 cm³ of 4% H₂/argon because of a decreased risk of damage to platinum elements in the instrument.

2.2. Tensile Testing. Tensile testing was performed on untreated, oxidized, and annealed single MA silk fibers using a Nano Bionix tensile tester (KLA Tencor, USA) and untreated, oxidized, and annealed single PAN fibers using an Electroforce 3200 (TA Instruments, USA) with a 2 mm gauge length. Untreated, oxidized, and annealed PAN fibers as well as untreated MA silk fibers were adhered to cardstock mounts using cyanoacrylate adhesives (Figure 2), while oxidized and annealed MA silk fibers remained mounted on the aluminum foil from the annealing procedure. These mounts were placed in tensile grips and their edges either cut with scissors or burnt through using a pyrography pen, leaving only the fiber spanning the gauge length. Fibers were extended at a constant semiquasi static strain rate of 10⁻² s⁻¹ under ambient conditions until failure. Stress and strain were calculated from the force and extension data. While it is common to use true stress and strain when studying elastomeric polymers such as silks,¹⁷ engineering stress provided a better comparison given the noncircular cross section of PAN fibers. TestWorks 4.0 software (MTS Corp., USA) was used to visualize the resulting stress–strain curves and calculate the Young's modulus from the initial slope of the elastic region of the stress–strain curves.

2.3. Scanning Electron Microscopy. MA silk fiber diameters were measured in ImageJ (National Institutes of Health) using scanning electron microscopy (SEM) (XL30-FEG, Philips, USA and Mira3, Tescan, Czech Republic) from at least three locations of one fiber out of every four used in tensile testing. Because PAN fiber cross sections are irregularly shaped, their average cross-sectional area ($N = 100$) was calculated from polished cross sections of fibers embedded in resin (Fiber Glast Development Corp., USA). Mounted samples for SEM were sputter-coated (Cressington 108 Auto, UK) for 15 s using a 20 mA current to create a thin layer of platinum (Pt) and palladium (Pd) for increased conductivity. To image fracture surfaces, Pt/Pd-coated fibers were mounted onto 45 or 90° aluminum pin stubs, so the fiber cross sections faced the electron beam.

2.4. Spectroscopy. Raman spectra of annealed fibers were acquired on a HORIBA LabRAM system using a 532 nm excitation

laser focused through a 100× objective. Laser power and exposure time were adjusted, so no burning was observed on the fibers. A linearly interpolated baseline correction with points at 900, 1800, 2400, and 3200 cm⁻¹ was performed, as the spectra had consistent baselines with little fluorescence. Spectra from 900 to 1800 cm⁻¹ were deconvoluted as 2–3 pseudo-voigt (70% Lorentzian, 30% Gaussian) peaks, representing ordered graphitic (G) and disordered (D) bands using OriginPro 2018 (Origin). Attenuated total reflectance–Fourier transform infrared (ATR–FTIR) spectra were collected from untreated, oxidized, and annealed fiber bundles with an Agilent Cary 630 spectrometer using a diamond ATR crystal and otherwise unprocessed. Raman mapping was performed on a HORIBA LabRAM system using a 473 nm laser focused through a 100× objective with a 300 nm spatial resolution. Linear background subtraction and peak fitting was performed using Origin with a Lorentzian function.

2.5. Wide-Angle X-ray Diffraction. Wide-angle X-ray diffraction (WAXD) patterns were collected from bundles of 1000–10,000 untreated, oxidized, and annealed MA silk and PAN fibers, along with a commercial carbon fiber (Hexcel), at the Soft Matter Interfaces beamline (12-ID) at Brookhaven National Laboratory, using a microfocused beam spot size of ~2 × 25 μm. Scattered X-rays were collected in a vacuum with a PILATUS3 300 kW detector (Dectris, Baden, Switzerland), consisting of 0.172 mm square pixels in a 1475 × 195 array.¹⁸ The beam energy was 16, 16.1, or 20 keV, and 3–5 different spots on the fiber bundles were interrogated. The detector was rotated, while maintaining a 275 mm distance from the samples to capture a wide Q range. Exposures (10–30 s) were taken at each detector angle, depending on fiber stability. Diffraction patterns from each detector angle were stitched together using custom software and then converted to intensity versus Q plots. These plots were radially averaged from $\phi = -10$ to 10, and a double exponential background subtraction was performed using Origin. Intensity versus ϕ plots were averaged over Q values that depended on the peak position and breadth, and a linear background was subtracted.

3. RESULTS AND DISCUSSION

MA silk underwent a rapid mass loss during oxidation beginning at 230 °C, while PAN cyclization and subsequent mass loss began at 242 °C (Figure 1). PAN in fiber or powder

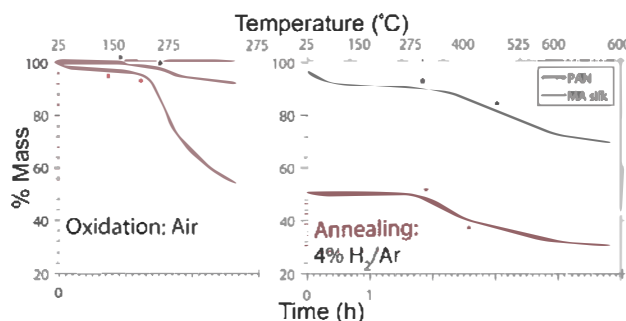


Figure 1. TGA of PAN and MA silk during the oxidation (air) and annealing (4% H₂/Ar) steps. Stars indicate inflection points at 162, 242, 316, and 482 °C in PAN and 145, 230, 298, and 411 °C in MA silk. Initial drops below 100 °C are likely the evaporation of adsorbed water vapor or other volatiles.

form tends to oxidize at a lower temperature than PAN films, likely due to the higher surface area to volume ratio.^{19–23} Minor mass losses at 162 and 145 °C were likely the combustion of volatile side chains in MA silk and additives in PAN, often carbonyl-containing units which are used to catalyze cyclization.^{5,6} These additives can shift the cyclization onset temperature compared to the PAN homopolymer. In MA silk, the abundance of nitrogen and the versatility of the

Table 1. Fiber Mass Loss and Shrinkage after Annealing

	property	untreated	oxidized	400 °C annealed	500 °C annealed	600 °C annealed
MA silk	avg fiber diameter (μm)	3.65 ± 0.33	3.04 ± 0.39	2.69 ± 0.44	2.56 ± 0.32	2.89 ± 0.59
	mass loss	N/A	44%	56%	62%	69%
PAN	avg fiber diameter (μm)	10.97 ± 1.08	11.60 ± 1.59	10.88 ± 1.07	10.00 ± 1.34	8.76 ± 1.58
	mass loss	N/A	1%	14%	20%	30%

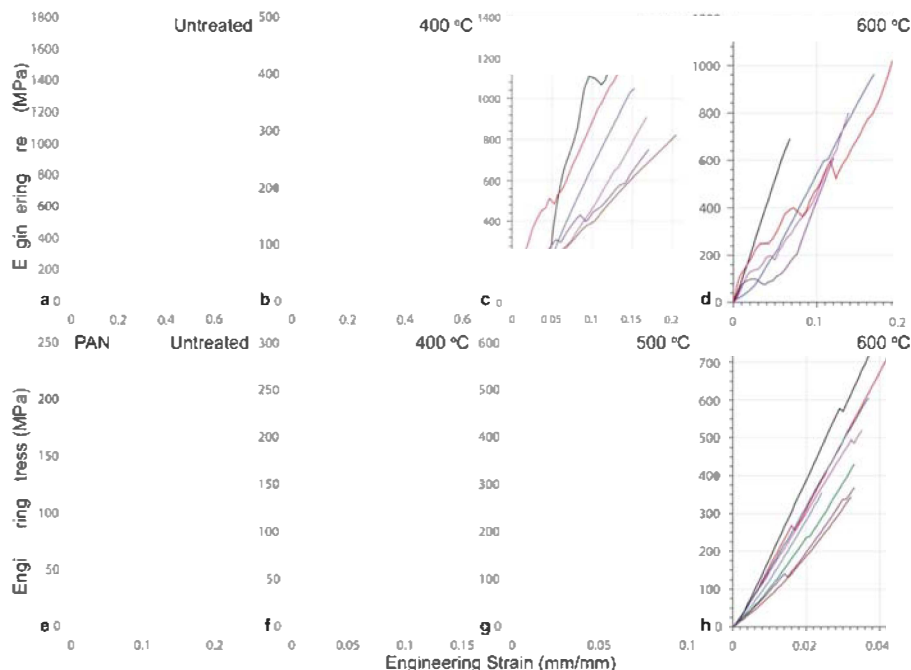


Figure 2. Stress–strain plots of untreated and annealed fibers. Each color in a plot represents a unique sample. Insets show a mounting setup of untreated MA silk (a–d) and all PAN fibers (e–h). Spikes in the stress–strain plots correspond to slippage in the grips.

Table 2. Fiber Mechanical Properties

annealing temperature	Young’s modulus (GPa)		ultimate tensile strength (MPa)		bulk toughness (J/cm^3)	
	MA silk	PAN	MA silk	PAN	MA silk	PAN
none	11.2 ± 2.1	2.50 ± 0.74	$1,430 \pm 270$	202 ± 49	501 ± 200	21.0 ± 9.5
400 °C	3.62 ± 1.6	3.68 ± 0.69	280 ± 120	186 ± 63	62.7 ± 41	9.92 ± 7.5
500 °C	8.03 ± 3.3	7.61 ± 1.5	908 ± 290	444 ± 100	$74.4 \pm 20.$	15.3 ± 6.3
600 °C	10.0 ± 3.1	15.9 ± 2.6	815 ± 170	503 ± 160	$52.2 \pm 30.$	8.53 ± 3.9

peptide carbonyl to cyclize with neighboring peptides likely enable cyclization to begin at a lower temperature and provides stability to silk fibers during the oxidation and annealing processes. Consequently, MA silk fibers maintained their shape and surface morphology after oxidation and annealing despite significant mass loss (Figure S1, Table 1). The variation in fiber diameters falls within an acceptable range for natural materials and is higher for 600 °C annealed fibers. Diameter variation will affect calculated stress values, yet no direct correlation is observed in this study. PAN fibers lost less mass, as their nitrile groups are incorporated into the cyclized structure rather than being released via oxidation similar to many side chains in oxygen-rich proteins.⁵

After annealing, MA silk fibers have a lower Young’s modulus, ultimate tensile strength, and toughness (Figure 2a–d, Table 2). Untreated MA silk has a sigmoidal stress–strain plot characterized by an initial linear elastic region, pseudoyield point, and stress hardening as the polyalanine domains are engaged until they fail, along with the peptide backbone.²⁴

Oxidized MA silk fibers had a Young’s modulus 3–20 times lower than untreated MA silk but with a wide spread in their stress–strain plots (Figure S2). Oxidized MA silk fibers usually broke immediately upon yielding, but some had a significant region of plastic deformation., MA silk annealed at 400 °C had a more consistent, slightly elastomeric behavior but a three-fold decrease in ultimate tensile strength compared with untreated MA silk (Figure 2). MA silk fibers annealed at 600 °C had a Young’s modulus equal to that of untreated silk but only half the ultimate strength and 1/10th the toughness. This behavior highlights the significant contribution of hydrogen bonding between structural motifs in MA silk, especially the “stick–slip” mechanism in the polyalanine nanocrystals, to MA silk’s strength and toughness.²⁴ The ability to hydrogen bond is lost as oxygen is burnt off and nitrogen is cyclized, as evidenced by a decreasing OH/NH stretch peak ca. 3200 cm^{-1} at annealing temperature (Figure 4a), resulting in weaker fibers. After oxidation, few cyclized regions are available to resist tensile loading. As these cyclized regions grow in size and

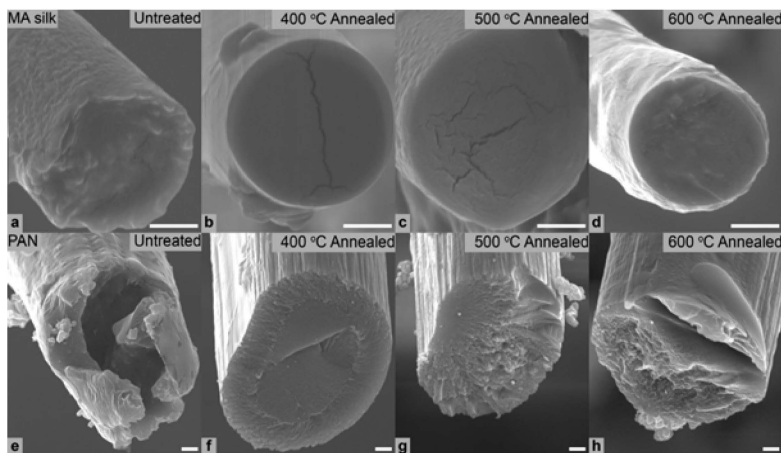


Figure 3. Untreated MA silk (a) and PAN (e) fibers have ductile fracture surfaces, fibers (400 °C) show a combination of ductile and brittle fracture, and fibers annealed at 500 and 600 °C show brittle fractures (b–d,f–h). Scale bars are 1 μm .

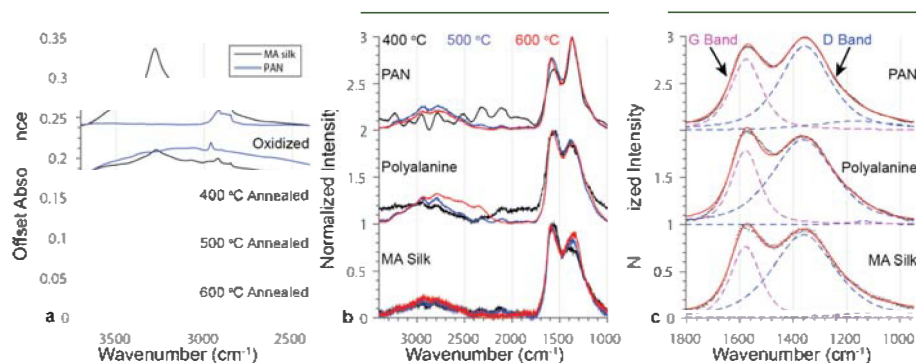


Figure 4. FTIR (a) and Raman (b) spectra of annealed MA silk, PAN, and polyaniline with deconvoluted and fitted spectra of 600 °C annealed materials (c).

the number during annealing and fuse adjacent spidroins, the fiber Young's modulus and strength increase.

Annealed PAN also transitioned from ductile to brittle failure, but its Young's modulus and ultimate strength increased more quickly than MA silk, when annealed above 500 °C, eclipsing that of the untreated polymer (Figure 2e–h). Despite polymer chain alignment in PAN crystals, little interaction is observed between neighboring chains, offering minimal slip resistance during tensile loading.⁴ The fusion of neighboring PAN chains begins during carbonization and continues during graphitization, which limits chain slip and stiffens the fibers. Comparing fibers annealed at 600 °C, PAN has a higher Young's modulus, but MA silk is stronger and tougher. This effect is likely due to structural differences between the annealed fibers and their different diameters. Larger fibers are more likely to contain defects which serve as crack initiators, and it is known that carbon fiber strength and modulus increase with decreasing fiber diameter.²⁵ Further studies must be conducted using fibers of similar diameters to more accurately compare their mechanical properties.

MA silk and PAN fiber fracture surfaces show a ductile-to-brittle transition with increasing annealing temperatures (Figure 3). A few oxidized and 400 °C annealed fibers showed necking, while others showed the outer shell of the fiber fracturing first and relaxing before ultimate failure in the bulk of the fiber (Figure S3). This 100–200 nm shell was visible in the annealed fibers through deflected cracks, differing contrast in the electron micrographs, and sword-in-sheath fracture

patterns (Figures 3b,c, S2).^{26,27} Core–shell structures are characteristic of carbon fibers, forming during oxidation as the shell oxidizes more rapidly and limits oxygen diffusion into the core.^{28–30} This phenomenon is apparent in oxidized and 400 °C annealed PAN, but the dominance of shear fracture at higher temperatures makes observing any core–shell structure in annealed PAN difficult (Figures 3, S4). Mirror mist hackle and shear fracture surfaces (Figure 3g,h) suggest that annealed PAN is more brittle than annealed MA silk.^{26,27}

Researchers have suggested that MA silk has an inherent core–shell structure largely comprised of two proteins, MA spidroins (MaSp) 1 and 2, which could contribute to the observed phenomenon.^{31,32} MaSp 1 has more polyaniline nanocrystals while MaSp 2 has more helical secondary structures, thus, researchers have hypothesized that MaSp 1 is stiffer.^{33–36} The fiber core contains both MaSp 1 and 2, but the 300–400 nm fiber shell may only contain MaSp 1. Since there are more polyaniline nanocrystals in MaSp 1 to act as templates for graphite formation, more graphitization is expected to occur in the shell. This hypothesis is supported by the fracture surface micrographs, as stiffness should increase with higher graphite density, resulting in crack deflection at the core–shell interface due to their different stiffnesses. Raman spectroscopy can be used to determine graphite content and crystal size by comparing the intensity (I) of the disordered (D) and graphitic (G) bands.^{37,38} Raman maps of MA silk fibers and PAN annealed at different temperatures suggest that the 100–300 nm fiber shell is more graphitic, with I_D/I_G ratios

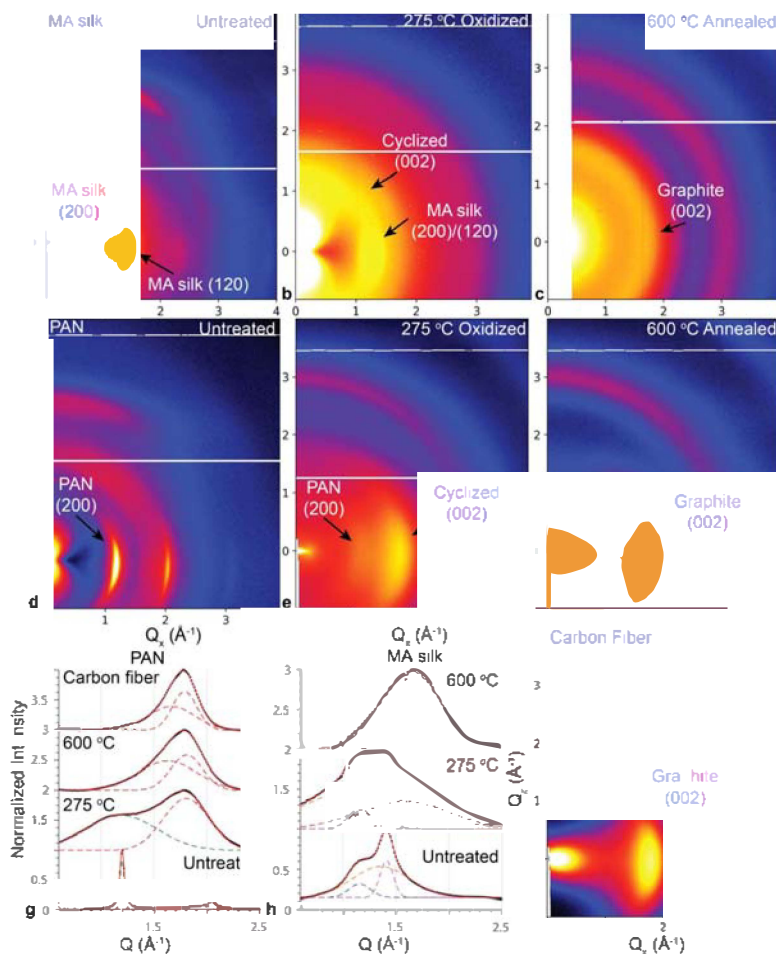


Figure 5. WAXD patterns of annealed silks, PAN, and commercial carbon fiber. Radially averaged plots from $\phi = -10$ to 10 highlight the PAN (200), MA silk (200) and (120), and graphite (002) diffraction peaks.

of ~ 1.2 and 0.8 for PAN core and shell, respectively, and ~ 0.8 and 0.2 for silk core and shell, respectively. This data implies both the spidroin distribution and annealing process contribute to forming a core-shell graphitic structure (Figure S5). However, due to low Raman signal and overlapping peaks caused by resin in which fibers are embedded, further studies are required to confirm and differentiate the two causes of this core-shell graphitization.

MA silk, PAN, and polyalanine powder graphitized to a similar extent upon annealing based on I_D/I_G , with no clear trend related to annealing temperature (Figures 4, S5, Table S1). The sharp amide band, which is present in Raman spectra of untreated MA silk at 1670 cm^{-1} , would appear as a shoulder in the G band if present (Figure S5). Its absence in both Raman and FTIR spectra coupled with broad peaks in the fingerprint region similar to those found in oxidized PAN suggest the peptide backbone is cyclized in a similar fashion (Figure S6).²¹ While vibrations of the ordered graphite lattice give rise to the singular G band, multiple vibrations from disordered regions, such as edges, voids, heteroatoms, or topological defects, make up the D band. Our results agree with previous works which suggest multiple D bands, especially in pyrolyzed materials.³⁹ As these defects are combusted and neighboring cyclized chains fused, there is less defect variety and larger graphite crystals. Natural polymers like silks have a less homogenous structure and more potential for many D

bands. The high I_D/I_G ratios, breadth of the bands, and presence of multiple, broad 2D bands suggest the fibers are mostly amorphous carbon with turbostratic graphite nanocrystals.^{39,40} The graphite crystals likely contain nitrogen impurities, as the fibers were not annealed at temperatures high enough to combust nitrogen.⁵

I_D/I_G is inversely proportional to the graphite crystal size and can be used to estimate it as a one-dimensional parameter using the Tuinstra-Koenig relationship $I_D/I_G = C_\lambda/L_\alpha$, where L_α is the crystallite size and C_λ is a prefactor coefficient that depends on the laser wavelength.^{37,41–43} Using this relationship, estimated graphite crystal sizes range from 3.7 to 5.5 nm for bulk fibers and 2.5 to $\sim 10\text{ nm}$ for fiber cross sections. The Tuinstra-Koenig approximation becomes less reliable for crystals below 2 nm , where the proportionality between L_α and I_D/I_G changes.^{44,45} Consequently, the correlation between I_D/I_G values and crystal size becomes discontinuous, and alternate methods of measuring crystal size are required.

X-ray diffraction is a more widely used method for determining crystal size and has been used to correlate I_D/I_G to graphite crystal size.^{37,38,45} WAXD with an area detector has the additional benefit of revealing crystal alignment within fibers. WAXD of untreated PAN and MA silk fibers showed sharp arcs, indicating preferential crystalline alignment along the length of the fiber (Figures 5a,d and 6a,d), due largely to the drawing process during extrusion.^{10,47} Crystals in PAN are

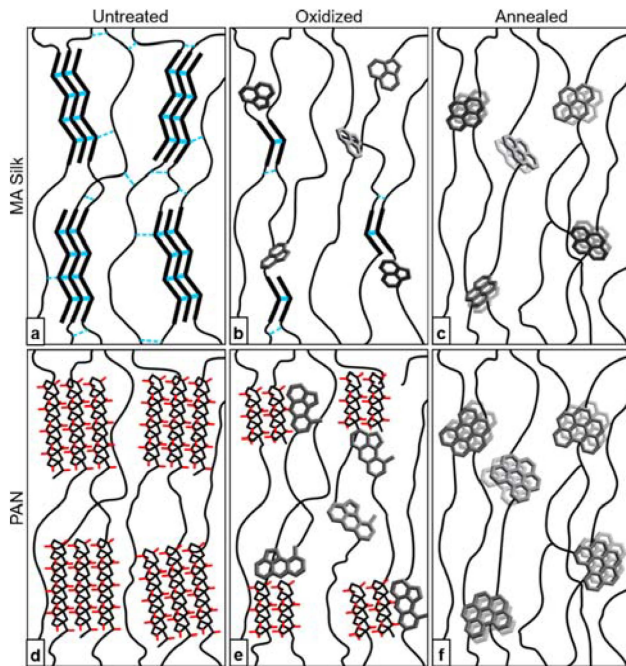


Figure 6. Schematic depicting graphite formation in annealed MA silk (a–c) and PAN (d–f). Polyaniline β -sheet nanocrystals and amorphous regions of MA silk are aligned through hydrogen bonding [(a), dashed blue lines]. PAN crystals contain neighboring chains aligned closely with the long axis with the fiber in either a planar zigzag or helical conformation (d). During oxidation, few, smaller polyaniline or PAN crystals remain, while small, cyclized domains form (b,e). These are aligned in PAN but not in MA silk because of significantly reduced hydrogen bonding. After annealing at 600 °C, graphite nanocrystals form, maintaining the alignment seen after oxidation (c,f).

larger but have a lower number density than in MA silk, which is one contributing factor to silk's superior strength.^{14,48} Oxidized PAN and MA silk both showed remnants of the untreated peaks, suggesting that some native crystals remain aligned but uncyclized or that cyclization begins on the crystal faces and is a slow process.⁴⁹ A peak close to the graphite (002) Q appears in oxidized PAN and MA silk, likely arising from the (002) planes of cyclized crystals (Figure 5g,h). The cyclized crystals which formed in MA silk were unaligned, producing uniform scattering across the detector visible as a ring (Figures 5b, 6b). Conversely, the PAN (200) reflection shrank as the graphite (002) increased, both maintaining similar alignment (Figure 5e). Vertical scattering at 0.1–0.5 \AA^{-1} is from the beamstop (Figure 5b,d).

There are two main theories for the crystal structure of PAN; both agree that the polymer chains aggregate parallel to each other and the long axis of the fiber, but there is disagreement over the chains folding as a planar zigzag or spiral conformation with the nitrile groups pointing outward along the (200) plane.^{4,48,50–53} Because cyclization converts nitrile groups to aromatic rings, which then stack to form graphite, a direct translation from PAN (200) to graphite (002) is possible. The exact reaction pathways during PAN oxidation have yet to be confirmed experimentally, but this evidence suggests that the cyclization occurs along the c -axis of PAN crystals, forming cyclized regions roughly parallel to the fiber axis (Figure 6e). Further in situ studies should be performed to confirm this process.

As annealing temperature increased, the cyclized structures became larger and more densely packed, indicated by sharper diffraction peaks (Figures 5c,f, 6c,f). Annealed PAN and carbon fiber had slightly larger graphite crystals than annealed MA silk (Table 3), as estimated using the graphite (002) peak

Table 3. Graphite Crystal Properties

	MA silk 600 °C	PAN 600 °C	carbon fiber
Q (\AA^{-1})	1.65	1.82	1.78
crystal size (nm)	1.80	3.38	3.78
Herman's orientation factor	0.041	0.616	0.803

through the Scherrer approximation, $L_{\alpha} = K\lambda/w \cos \theta$. λ is the X-ray wavelength, K is a constant of 0.9 based on the type of unit cell, θ is the diffracted peak position, and w is the peak full width at half-maximum.⁴⁶ The graphite (002) Q value in every material tested is notably less than that of pure graphite, 1.872 \AA^{-1} , which is characteristic of turbostratic graphite and likely a result of the low annealing temperatures and nitrogen inclusions.⁵⁴ Annealed PAN and the carbon fiber control had the most densely packed graphite, and their (002) diffraction deconvoluted to two peaks instead of the one peak present in MA silk. The additional peak is broader and at a lower Q , similar to that of MA silk, but is textured along the horizontal as the (002) graphite peak in annealed PAN. It could represent graphite formed from amorphous regions of the PAN that also aligns along the fiber axis.

Graphite in annealed PAN and the carbon fiber control shows a preferential alignment along the length of the fiber, unlike MA silk (Figures 5c,f, S7). As the graphite in MA silk is randomly oriented, it scatters X-rays in a ring instead of a sharp arc.⁵⁵ This effect is quantified using Herman's orientation function, $f_c = \frac{3}{2}(\langle \cos^2 \phi \rangle - 1)$, where ϕ is the azimuthal angle and $\langle \cos^2 \phi \rangle$ is the weighted average of $\cos^2 \phi$ based on the intensity (I) as a function of ϕ , $\frac{\int_0^{\pi/2} I(\phi) \sin \phi \cos^2 \phi}{\int_0^{\pi/2} I(\phi) \sin \phi}$.^{55,56}

Annealed MA silk showed no preferred graphite orientation (Table 3, Figure S8), while the degree of alignment increased in PAN proportional to the annealing temperature, with the carbon fiber control as the highest. Horizontal scattering at 0.1–0.5 \AA^{-1} in annealed PAN and carbon fiber is due to the graphite alignment (Figure 5f,i), but the intensity of the circular scattering in annealed MA silk is so high that this feature cannot be observed if it is present. Previous studies have shown that carbon fibers produce both types of scattering in the 0.1–0.5 \AA^{-1} range.^{57,58}

4. CONCLUSIONS

Although the polyaniline β -sheet nanocrystals in MA silk may be good templates for graphite formation, that alone is not sufficient to produce better carbon fibers than PAN. A major contributing factor is their loss of alignment upon oxidation and annealing. Multiple works suggest that hydrogen bonding plays a crucial role in maintaining spidroin and polyaniline alignment, which is disrupted with the loss of $-\text{OH}$ groups and cyclization of the peptide N.^{13,14,24,59} The loss of hydrogen bonding throughout the fiber disrupts the secondary-quaternary structure of the spidroins and removes MA silk's primary load-bearing mechanism. Nonoriented polyaniline nanocrystals, even if they are cyclized to small graphitic

domains, cannot offer an appreciable resistance to tensile fracture.

For polymers, natural or otherwise, to produce carbon fiber of a similar quality as PAN, they cannot rely on hydrogen bonding for structural stability or contain a high mass fraction of oxygen, lest they shrink to an unusable extent. A direct pathway, without significant molecular rearrangement or combustion, to form graphite from existing crystals in the polymer is useful in maintaining alignment, as observed with PAN. Given high enough temperatures, the graphite crystals in PAN can grow by accumulating amorphous parts of the polymer, while maintaining sufficient amorphous carbon to keep the fibers intact. One common strategy to create graphitic fibers is to include cyclic or aromatic structures into a precursor fiber, but this often leaves no mechanism for the fusion of separate polymer chains, likely limiting the overall extent of graphitization.⁹ Polyaniline-like domains could be incorporated into block copolymers for biomimetic graphite precursors. However, careful attention must be paid to the graphitization mechanisms of the other blocks with intentional design to maximize the bonding between neighboring polymer chains and the eventual formation of graphite aligned along the fiber.

■ AUTHOR INFORMATION

Corresponding Author

David J. Kisailus – *Materials Science and Engineering Program and Department of Chemical and Environmental Engineering, University of California, Riverside, Riverside, California 92521, United States*; orcid.org/0000-0001-9976-485X;
Email: david@engr.ucr.edu

Authors

Thomas W. Dugger – *Materials Science and Engineering Program, University of California, Riverside, Riverside, California 92521, United States*

Sourangsu Sarkar – *Department of Chemical and Environmental Engineering, University of California, Riverside, Riverside, California 92521, United States*

Sandra M. Correa-Garhwal – *Department of Evolution, Ecology, and Organismal Biology, University of California, Riverside, Riverside, California 92521, United States*

Mikhail Zhernenkov – *National Synchrotron Light Source II, Brookhaven National Laboratory, Upton, New York 11973-5000, United States*; orcid.org/0000-0003-3604-0672

Yugang Zhang – *National Synchrotron Light Source II, Brookhaven National Laboratory, Upton, New York 11973-5000, United States*

Gitanjali Kolhatkar – *Nanoelectronics-Nanophotonics, Institut National de la Recherche Scientifique, Université du Québec, Varennes J3X1S2, Québec, Canada*; orcid.org/0000-0003-0848-4751

Ramya Mohan – *Materials Science and Engineering Program, University of California, Riverside, Riverside, California 92521, United States*

Luz Cruz – *Materials Science and Engineering Program, University of California, Riverside, Riverside, California 92521, United States*

Aura D. Lubio – *Nanoelectronics-Nanophotonics, Institut National de la Recherche Scientifique, Université du Québec, Varennes J3X1S2, Québec, Canada*

Andreas Ruediger – *Nanoelectronics-Nanophotonics, Institut National de la Recherche Scientifique, Université du Québec, Varennes J3X1S2, Québec, Canada*

Cheryl Y. Hayashi – *Materials Science and Engineering Program and Department of Evolution, Ecology, and Organismal Biology, University of California, Riverside, Riverside, California 92521, United States*; *Division of Invertebrate Zoology and Sackler Institute for Comparative Genomics, American Museum of Natural History, New York, New York 10024-5192, United States*

Kathryn E. Urich – *Materials Science and Engineering Program and Department of Chemistry, University of California, Riverside, Riverside, California 92521, United States*; orcid.org/0000-0001-7273-7528

Author Contributions

The manuscript was written through contributions of all authors. All authors have given approval to the final version of the manuscript.

Funding

The authors would like to acknowledge funding for this research from AFSOR Multi-University Research Initiative: FA9550-15-1-0009 and ARO DURIPs: W911NF-16-1-0208 and W911NF-14-1-0427. This material is based upon work supported by the National Science Foundation Graduate Research Fellowship Program under grant no. DGE-1326120. Any opinions, findings, and conclusions or recommendations expressed in this material are those of the author(s) and do not necessarily reflect the views of the National Science Foundation.

■ ACKNOWLEDGMENTS

This research used the SMI beamline (12-ID) of the National Synchrotron Light Source II, a U.S. Department of Energy (DOE) Office of Science User Facility operated for the DOE Office of Science by Brookhaven National Laboratory under Contract No. DE-SC0012704. The authors would like to acknowledge the Central Facility for Advanced Microscopy and Microanalysis at UC Riverside for use of their XL-30 SEM, and Prof. Satish Kumar for helpful discussion and providing small diameter PAN fibers.

■ REFERENCES

(1) Holcomb, G. Carbon Fiber & Graphene Manufacturing in the US. IBISWorld Ind. Rep. OD4649 [Online]. October 29, 2019, pp 3–

15. IBISWorld. www.ibisworld.com/us/en/industry-specialized/od4649 (accessed November 2019).
- (2) Zweben, C. *Mechanical Engineers' Handbook*; Kutz, M., Ed.; Wiley: Hoboken, NJ, 2015; Vol. 1, Chapter 10, pp 1–37.
- (3) Chung, D. Carbon Fibers, Nanofibers, and Nanotubes. *Carbon Composites*, 2nd ed.; Elsevier Science: Saint Louis, 2016; pp 12–47.
- (4) Fitzer, E. Pan-Based Carbon Fibers—Present State and Trend of the Technology from the Viewpoint of Possibilities and Limits to Influence and to Control the Fiber Properties by the Process Parameters. *Carbon* **1989**, *27*, 621–645.
- (5) Rahaman, M. S. A.; Ismail, A. F.; Mustafa, A. A Review of Heat Treatment on Polyacrylonitrile Fiber. *Polym. Degrad. Stab.* **2007**, *92*, 1421–1432.
- (6) Park, S.-J.; Heo, G.-Y. Precursors and Manufacturing of Carbon Fibers. *Carbon Fibers*; Springer Netherlands: Dordrecht, 2015; Vol. 210, pp 31–66.
- (7) Gandini, A. Polymers from Renewable Resources: A Challenge for the Future of Macromolecular Materials. *Macromolecules* **2008**, *41*, 9491–9504.
- (8) Liu, H. C.; Chien, A.-T.; Newcomb, B. A.; Liu, Y.; Kumar, S. Processing, Structure, and Properties of Lignin- and CNT-Incorporated Polyacrylonitrile-Based Carbon Fibers. *ACS Sustainable Chem. Eng.* **2015**, *3*, 1943–1954.
- (9) Souto, F.; Calado, V.; Pereira, N. Lignin-Based Carbon Fiber: A Current Overview. *Mater. Res. Express* **2018**, *5*, 072001.
- (10) Vollrath, F.; Knight, D. P. Liquid Crystalline Spinning of Spider Silk. *Nature* **2001**, *410*, 541–548.
- (11) Babb, P. L.; Lahens, N. F.; Correa-Garhwal, S. M.; Nicholson, D. N.; Kim, E. J.; Hogenesch, J. B.; Kuntner, M.; Higgins, L.; Hayashi, C. Y.; Agnarsson, I.; Voight, B. F. The Nephila Clavipes Genome Highlights the Diversity of Spider Silk Genes and Their Complex Expression. *Nat. Genet.* **2017**, *49*, 895–903.
- (12) Lewis, R. V. Spider Silk: Ancient Ideas for New Biomaterials. *Chem. Rev.* **2006**, *106*, 3762–3774.
- (13) Keten, S.; Xu, Z.; Ihle, B.; Buehler, M. J. Nanoconfinement Controls Stiffness, Strength and Mechanical Toughness of β -Sheet Crystals in Silk. *Nat. Mater.* **2010**, *9*, 359–367.
- (14) Sampath, S.; Isdebski, T.; Jenkins, J. E.; Ayon, J. V.; Henning, R. W.; Orgel, J. P. R. O.; Antipoa, O.; Yarger, J. L. X-Ray Diffraction Study of Nanocrystalline and Amorphous Structure within Major and Minor Ampullate Dragline Spider Silks. *Soft Matter* **2012**, *8*, 6713.
- (15) Cho, S. Y.; Yun, Y. S.; Lee, S.; Jang, D.; Park, K.-Y.; Kim, J. K.; Kim, B. H.; Kang, K.; Kaplan, D. L.; Jin, H.-J. Carbonization of a Stable β -Sheet-Rich Silk Protein into a Pseudographitic Pyroprotein. *Nat. Commun.* **2015**, *6*, 7145.
- (16) Kuntner, M.; Hamilton, C. A.; Cheng, R.-C.; Gregorič, M.; Lupše, N.; Lokovšek, T.; Lemmon, E. M.; Lemmon, A. R.; Agnarsson, I.; Coddington, J. A.; Bond, J. E.; Paterson, A. Golden Orbweavers Ignore Biological Rules: Phylogenomic and Comparative Analyses Unravel a Complex Evolution of Sexual Size Dimorphism. *Syst. Biol.* **2019**, *68*, 555–572.
- (17) Blackledge, T. A.; Summers, A. P.; Hayashi, C. Y. Gumfooted Lines in Black Widow Cobwebs and the Mechanical Properties of Spider Capture Silk. *Zoology* **2005**, *108*, 41–46.
- (18) Zhernenkov, M. Soft Matter Interfaces Beamline at NSLS-II: Geometrical Ray-Tracing vs. Wavefront Propagation Simulations. In *Advances in Computational Methods for X-ray Optics III*; del Rio, M. S., Chubar, O., Eds.; Brookhaven National Laboratory, 2014; Vol. 9209.
- (19) Xue, T. J.; McKinney, M. A.; Wilkie, C. A. The Thermal Degradation of Polyacrylonitrile. *Polym. Degrad. Stab.* **1997**, *58*, 193–202.
- (20) Wang, Y.; Xu, L.; Wang, M.; Pang, W.; Ge, X. Structural Identification of Polyacrylonitrile during Thermal Treatment by Selective ^{13}C Labeling and Solid-State ^{13}C NMR Spectroscopy. *Macromolecules* **2014**, *47*, 3901–3908.
- (21) Cipriani, E.; Zanetti, M.; Bracco, P.; Brunella, V.; Luda, M. P.; Costa, L. Crosslinking and Carbonization Processes in PAN Films and Nanofibers. *Polym. Degrad. Stab.* **2016**, *123*, 178–188.
- (22) Tang, H.; Chen, W.; Wang, J.; Dugger, T.; Cruz, L.; Kisailus, D. Electrochemical N-Doped Graphitic Nanofiber - Metal/Metal Oxide Nanoparticle Composites. *Small* **2018**, *14*, 1703459.
- (23) Szepcsik, B.; Pukánszky, B. The Mechanism of Thermal Stabilization of Polyacrylonitrile. *Thermochim. Acta* **2019**, *671*, 200–208.
- (24) Keten, S.; Buehler, M. J. Nanostructure and Molecular Mechanics of Spider Dragline Silk Protein Assemblies. *J. R. Soc., Interface* **2010**, *7*, 1709–1721.
- (25) Jones, B. F.; Duncan, R. G. The Effect of Fibre Diameter on the Mechanical Properties of Graphite Fibres Manufactured from Polyacrylonitrile and Rayon. *J. Mater. Sci.* **1971**, *6*, 289–293.
- (26) Faber, K. T.; Evans, A. G. Crack Deflection Processes—I. Theory. *Acta Metall.* **1983**, *31*, 565–576.
- (27) Faber, K. T.; Evans, A. G. Crack Deflection Processes—II. Experiment. *Acta Metall.* **1983**, *31*, 577–584.
- (28) Lv, M.-y.; Ge, H.-y.; Chen, J. Study on the Chemical Structure and Skin-Core Structure of Polyacrylonitrile-Based Fibers during Stabilization. *J. Polym. Res.* **2009**, *16*, 513–517.
- (29) Guo, X.; Cheng, Y.; Fan, Z.; Feng, Z.; He, L.; Liu, R.; Xu, J. New Insights into Orientation Distribution of High Strength Polyacrylonitrile-Based Carbon Fibers with Skin-Core Structure. *Carbon* **2016**, *109*, 444–452.
- (30) Nunna, S.; Creighton, C.; Hameed, N.; Naebe, M.; Henderson, L. C.; Setty, M.; Fox, B. L. Radial Structure and Property Relationship in the Thermal Stabilization of PAN Precursor Fibres. *Polym. Test.* **2017**, *59*, 203–211.
- (31) Vollrath, F.; Holtet, T.; Thøgersen, H. C.; Frische, S. Structural Organization of Spider Silk. *Proc. R. Soc. London, Ser. B* **1996**, *263*, 147–151.
- (32) Spöner, A.; Vater, W.; Monajembashi, S.; Unger, E.; Grosse, F.; Weisshart, K. Composition and Hierarchical Organisation of a Spider Silk. *PLoS One* **2007**, *2*, No. e998.
- (33) Hayashi, C. Y.; Shipley, N. H.; Lewis, R. V. Hypotheses That Correlate the Sequence, Structure, and Mechanical Properties of Spider Silk Proteins. *Int. J. Biol. Macromol.* **1999**, *24*, 271–275.
- (34) Rising, A.; Nimmervoll, H.; Grip, S.; Fernandez-Arias, A.; Storckenfeldt, E.; Knight, D. P.; Vollrath, F.; Engström, W. Spider Silk Proteins – Mechanical Property and Gene Sequence. *Zool. Sci.* **2005**, *22*, 273–281.
- (35) Brooks, A. Distinct Contributions of Model MaSp1 and MaSp2 like Peptides to the Mechanical Properties of Synthetic Major Ampullate Silk Fibers as Revealed in Silico. *Nanotechnol. Sci. Appl.* **2008**, *1*, 9–16.
- (36) Tokareva, O.; Michalczechen-Lacerda, V. A.; Rech, E. L.; Kaplan, D. L. Recombinant DNA Production of Spider Silk Proteins: Recombinant Spider Silks. *Microb. Biotechnol.* **2013**, *6*, 651–663.
- (37) Tuinstra, F.; Koenig, J. L. Raman Spectrum of Graphite. *J. Chem. Phys.* **1970**, *53*, 1126–1130.
- (38) Knight, D. S.; White, W. B. Characterization of Diamond Films by Raman Spectroscopy. *J. Mater. Res.* **1989**, *4*, 385–393.
- (39) Merlen, A.; Buijnsters, J.; Pardanaud, C. A Guide to and Review of the Use of Multiwavelength Raman Spectroscopy for Characterizing Defective Aromatic Carbon Solids: From Graphene to Amorphous Carbons. *Coatings* **2017**, *7*, 153.
- (40) Ferrari, A. C.; Robertson, J. Raman Spectroscopy of Amorphous, Nanostructured, Diamond-like Carbon, and Nanodiamond. *Philos. Trans. R. Soc., A* **2004**, *362*, 2477–2512.
- (41) Matthews, M. J.; Pimenta, M. A.; Dresselhaus, G.; Dresselhaus, M. S.; Endo, M. Origin of Dispersive Effects of the Raman D Band in Carbon Materials. *Phys. Rev. B* **1999**, *59*, R6585–R6588.
- (42) Chu, P. K.; Li, L. Characterization of Amorphous and Nanocrystalline Carbon Films. *Mater. Chem. Phys.* **2006**, *96*, 253–277.
- (43) Ferrari, A. C. Raman Spectroscopy of Graphene and Graphite: Disorder, Electron–Phonon Coupling, Doping and Nonadiabatic Effects. Raman spectroscopy of graphene and graphite: Disorder, electron-phonon coupling, doping and nonadiabatic effects. *Solid State Commun.* **2007**, *143*, 47–57.

- (44) Ferrari, A. C.; Robertson, J. Interpretation of Raman Spectra of Disordered and Amorphous Carbon. *Phys. Rev. B* **2000**, *61*, 14095–14107.
- (45) Zickler, G. A.; Smarsly, B.; Gierlinger, N.; Peterlik, H.; Paris, O. A Reconsideration of the Relationship between the Crystallite Size L_a of Carbons Determined by X-Ray Diffraction and Raman Spectroscopy. *Carbon* **2006**, *44*, 3239–3246.
- (46) Langford, J. I.; Wilson, A. J. C. Scherrer after Sixty Years: A Survey and Some New Results in the Determination of Crystallite Size. *J. Appl. Crystallogr.* **1978**, *11*, 102–113.
- (47) Tsai, J.-S. Effect of Drawing Ratio during Spinning and Oxidation on the Properties of Polyacrylonitrile Precursor and Resulting Carbon Fibre. *J. Mater. Sci. Lett.* **1992**, *11*, 140–142.
- (48) Colvin, B. G.; Storr, P. The Crystal Structure of Polyacrylonitrile. *Eur. Polym. J.* **1974**, *10*, 337–340.
- (49) Glišović, A.; Salditt, T. Temperature Dependent Structure of Spider Silk by X-Ray Diffraction. *Appl. Phys. A* **2007**, *87*, 63–69.
- (50) Stéfani, R.; Chevreton, M.; Garnier, M.; Eyraud, C. Les Structures Cristallines Du Polyacrylonitrile. In *Comptes rendus Hebdomadaires des Séances de l'Académie des Sciences*; Gauthier-Villars, Ed.; Académie des Sciences, 1960; Vol. 251, pp 2174–2176.
- (51) Bohn, C. R.; Schaeffgen, J. R.; Statton, W. O. Laterally Ordered Polymers: Polyacrylonitrile and Poly(Vinyl Trifluoroacetate). *J. Polym. Sci.* **1961**, *55*, 531–549.
- (52) Karbownik, I.; Fiedot, M.; Rac, O.; Suchorska-Woźniak, P.; Rybicki, T.; Teterycz, H. Effect of Doping Polyacrylonitrile Fibers on Their Structural and Mechanical Properties. *Polymer* **2015**, *75*, 97–108.
- (53) Eom, Y.; Park, Y.; Jung, Y. M.; Kim, B. C. Effects of Conformational Change of Polyacrylonitrile on the Aging Behavior of the Solutions in N,N-Dimethyl Formamide. *Polymer* **2017**, *108*, 193–205.
- (54) Li, Z. Q.; Lu, C. J.; Xia, Z. P.; Zhou, Y.; Luo, Z. X-Ray Diffraction Patterns of Graphite and Turbostratic Carbon. *Carbon* **2007**, *45*, 1686–1695.
- (55) Alexander, L. Preferred Orientation in Polymers. *X-ray Diffraction Methods in Polymer Science*; John Wiley & Sons, Inc.: New York, 1969; pp 199–268.
- (56) Hermans, P. H. X-Ray Studies on Orientation. In *Contribution to the Physics of Cellulose Fibers*; Houwink, I. R., Ketelaar, J. A. A., Eds.; Elsevier Publishing Company, Inc: Amsterdam, 1946; pp 158–187.
- (57) Tang, M. Y.; Rice, G. G.; Fellers, J. F.; Lin, J. S. X-ray Scattering Studies of Graphite Fibers. *J. Appl. Phys.* **1986**, *60*, 803–810.
- (58) Gupta, A.; Harrison, I. R.; Lahijani, J. Small-Angle X-Ray Scattering in Carbon Fibers. *J. Appl. Crystallogr.* **1994**, *27*, 627–636.
- (59) van Beek, J. D.; Hess, S.; Vollrath, F.; Meier, B. H. The Molecular Structure of Spider Dragline Silk: Folding and Orientation of the Protein Backbone. *Proc. Natl. Acad. Sci. U.S.A.* **2002**, *99*, 10266–10271.